RSC Advances

PAPER

View Article Online
View Journal | View Issue

Cite this: *RSC Adv.*, 2025, **15**, 32041

Polypyrrole functionalized ($Ti_3C_2T_x$–SnO_2 NPs) nanocomposite-based hybrid capacitive electrode for electrochemical detection of *Klebsiella pneumoniae*

Md. Abdul Khaleque,[ab] Moumita Rahman Sazza,[c] Selina Akter,[c] Md. Romzan Ali,[ab] Syed Imdadul Hossain,[bd] Rahman Saidur,[ef] Mohamed Aly Saad Aly *[bgh] and Md. Zaved H. Khan *[ab]

Bacterial detection is crucial for accurate clinical diagnostics and effective environmental monitoring. Particularly, *Klebsiella pneumoniae*, a pathogenic bacterium, can cause a wide range of infections, including meningitis, bloodstream infections, pneumonia, urinary tract infections, and wound or surgical site infections. Herein, a polypyrrole (PPy) functionalized $Ti_3C_2T_x$–tin dioxide nanoparticle (SnO_2 NPs) nanocomposite-based hybrid capacitive electrode for the electrochemical detection of *Klebsiella pneumoniae* ATCC 700603 is developed. The PPy layer was coated onto the $Ti_3C_2T_x$–SnO_2 NPs *via* drop-casting, followed by immobilization of bacteriophages through a potentiostatic, charge-directed chronoamperometric approach. The resulting $Ti_3C_2T_x$–SnO_2 NPs/PPy/phage biosensor exhibited a wide dynamic detection range of 10 to 10^6 CFU mL^{-1}, with excellent linearity confirmed by differential pulse voltammetry and electrochemical impedance spectroscopy. The nanocomposite was characterized by using a suite of techniques including FTIR, XRD, elemental mapping, cyclic voltammetry, and galvanostatic charge–discharge to understand its composition, structure, and electrochemical properties. The developed $Ti_3C_2T_x$–SnO_2 NPs/PPy hybrid electrode demonstrated typical supercapacitor behavior with a specific capacitance of 806.67 F g^{-1} at 2.0 A g^{-1} of current density, and exhibited exceptional cycling stability, storing 98.3% of its capacitance after 10^4 consecutive cycles. The selectivity of the modified electrode to detect *K. pneumoniae* while minimizing interference from various bacterial cells was assessed, exhibiting remarkable resilience, and remaining unaffected. Additionally, after eleven successive weeks of storage, the proposed sensor showed no discernible reduction current (~98.1%), demonstrating an excellent stability. Despite the presence of background bacterial interference in the environmental sample, *K. pneumoniae* detection remained highly reliable and consistent with recovery efficiency ranging from 99.75 to 99.90%.

Received 23rd May 2025
Accepted 24th August 2025

DOI: 10.1039/d5ra03642a

rsc.li/rsc-advances

1 Introduction

Klebsiella pneumoniae (*K. pneumoniae*), is an opportunistic pathogen that causes severe infections, particularly in immunocompromised individuals, hospitalized patients, and those with chronic conditions.[1] The ATCC 700603 strain, originally isolated from a hospitalized patient in Virginia, is known for producing the SHV-18 β-lactamase enzyme, contributing to its extended-spectrum β-lactamase (ESBL) activity. It serves as a reference strain for ESBL detection and antimicrobial susceptibility testing.[2] This strain commonly causes hospital-acquired pneumonia, especially in chronic respiratory patients, urinary tract infections, bloodstream infections, and other conditions like meningitis and liver abscesses.[3] Other types of disease, including wound infections, endophthalmitis, and necrotizing fasciitis, are caused by these bacteria.[4]

[a]*Department of Chemical Engineering, Jashore University of Science and Technology, Jashore 7408, Bangladesh. E-mail: zaved.khan@just.edu.bd*
[b]*Laboratory of Nano-bio and Advanced Materials Engineering (NAME), Jashore University of Science and Technology, Jashore 7408, Bangladesh*
[c]*Department of Microbiology, Jashore University of Science and Technology, Jashore 7408, Bangladesh*
[d]*Centre for Sophisticated Instrumentation and Research Laboratory (CSIRL), Jashore University of Science and Technology, Jashore 7408, Bangladesh*
[e]*Research Centre for Nano-Materials and Energy Technology (RCNMET), School of Engineering and Technology, Sunway University, Bandar Sunway, Malaysia*
[f]*School of Engineering, Lancaster University, Lancaster LA1 4YW, UK*
[g]*School of Electrical and Computer Engineering, Georgia Institute of Technology, Atlanta, GA 30332, USA. E-mail: Mohamed.alysaadaly@ece.gatech.edu*
[h]*Department of Electrical and Computer Engineering at Georgia Tech Shenzhen Institute (GTSI), Shenzhen, Guangdong, 518055, China*

Symptoms vary by infection site and include fever, cough with bloody sputum, shortness of breath, painful urination, abdominal pain, chills, and confusion.[5] Therefore, there is a critical need for fast and precise detection of *K. pneumoniae* ATCC 700603 infections to enable timely antibiotic treatment. Early detection is crucial because these infections, especially those involving antibiotic-resistant strains, can be serious and require prompt intervention to improve patient outcomes. Furthermore, existing diagnostic methods often struggle with issues like inadequate sensitivity, selectivity, and long detection times.

Conventional detection of *K. pneumoniae* relies on microbiological techniques involving isolation and identification, which can be time-consuming and labor-intensive. DNA-based biosensors offer an alternative but have limitations such as complex fabrication, low stability, non-specific binding, high costs, and poor performance in complex samples like blood or environmental matrices.[6,7] These challenges restrict their practical use in clinical diagnostics and environmental monitoring. Enzyme-Linked Immunosorbent Assay (ELISA), widely used for antigen and antibody detection, is prone to cross-reactivity, which may cause false positives. Its accuracy depends heavily on the specificity of antibodies and the quality of reagents.[8] Similarly, polymerase Rhain reaction (PCR) is a highly sensitive method for amplifying DNA, but DNA extraction from clinical samples can be laborious.[9] Moreover, PCR cannot distinguish between live and dead pathogens, reducing its reliability in assessing active infections. In contrast, phage-based electrochemical biosensors present a promising alternative.[10] These biosensors leverage bacteriophages' natural specificity for their host bacteria, enabling rapid, sensitive, and cost-effective detection of viable pathogens. They are also easier to fabricate and can operate effectively in diverse sample conditions, making them suitable for both clinical and environmental applications.

Charge-directed immobilization of bacteriophages using chronoamperometry is essential for biosensor fabrication. This process enables the effective construction of bacteriophage-immobilized biorecognition elements for detecting target whole-cell bacteria.[11–14] In this process, applying a positive voltage to the sensor surface promotes the preferred orientation and stable attachment of bacteriophages, particularly those with positively charged tails and negatively charged heads.[15] Accordingly, the electrochemical capacitive properties promote efficient bacteriophage attachment and ensure its stable retention on the sensor surface.[16] In this study, PPy-functionalized capacitive electrode was engineered for efficient bacteriophage immobilization to detect *K. pneumoniae*. Similarly, Umer Farooq *et al.*,[17] used a bacterial cellulose-carbon nanotube nanocomposite modified with polyethyleneimine to detect *S. aureus* in milk at a 5.0 CFU mL^{-1} limit. Another study used a polyacrylonitrile-derived carbon nanofiber SPE to detect *E. coli*, achieving a 36 CFU mL^{-1} detection limit across 10^2–10^6 CFU mL^{-1}.[18] In this study, the PPy-functionalized electrode surface was modified with bacteriophages using a charge-directed chronoamperometry method for targeting *K. pneumoniae*. This approach offers a more straightforward alternative to previously reported biosensors.

The PPy composites exhibit excellent electrical properties and have been widely explored for applications in sensors,[19] energy storage,[20] electromagnetic interference (EMI) shielding,[21] pharmaceuticals,[22] and catalysis.[23] Enhancing PPy's electrochemical performance often involves "p-doping"-the introduction of dopant anions to improve conductivity and alter the material's morphology and physicochemical characteristics.[24] They are commonly synthesized by hydrothermal/solvothermal,[25] *in situ* growth,[26] solution mixing,[27] electrochemical deposition,[28] and layer-by-layer assembly.[29] Among the large family of 2D $Ti_3C_2T_x$ MXene, and owing to its large surface area, high electrical conductivity, and unique surface chemistry, $Ti_3C_2T_x$ is frequently cited as the most commonly used and versatile $Ti_3C_2T_x$ material for sensor applications,[30] supercapacitors,[31] Li–S batteries,[32] and Li-ion batteries[33] because of the active T_x group (*e.g.*, –O, –OH, and –F).[34] But, due to strong van der Waals interactions between the layers and hydrogen bonds, $Ti_3C_2T_x$ forms a stacking and aggregation film. Thus, $Ti_3C_2T_x$ is usually used to form composites with transition metals (*e.g.*, SnO_2, TiO_2, ZnO) and other electrochemically active materials.[35,36] Tin dioxide (SnO_2) is a key n-type semiconductor, depicted by its wide band gap (3.6 eV), high electron mobility (100–200 $cm^2\ V^{-1}\ s^{-1}$), and large exciton binding energy (130 meV), making it suitable for optoelectronic and sensing applications.[37] This research utilized hydrothermal methods to synthesize the $Ti_3C_2T_x$–SnO_2 nanocomposite. $Ti_3C_2T_x$ can act as a buffer layer to help move electrons across the composite and reduce the relatively low conductivity of SnO_2.[18] Furthermore, SnO_2 can enhance the structural integrity and cycle life of the electrodes.

A $Ti_3C_2T_x$–metal oxide–PPy hybrid composite enhances supercapacitor flexibility and performance by combining high conductivity with structural support. $Ti_3C_2T_x$ ensures conductivity and stability, while the metal oxide and PPy improve both conductivity and flexibility.[38] $Ti_3C_2T_x$ can achieve a specific capacitance of ~245 F g^{-1} in H_2SO_4 due to pseudocapacitance when stacking is avoided.[39,40] However, its inherent capacitance is limited and can be significantly enhanced by integrating redox-active materials to form synergistic composites. For instance, Liang Tong *et al.*,[41] developed a PPy/$Ti_3C_2T_x$ composite demonstrating exceptional electrochemical performance, with a specific capacitance of 420.2 F g^{-1} and remarkable cycling stability (86% capacitance retention after 10^4 charge–discharge cycles), representing a significant enhancement over the individual components. Chen Zhao *et al.*,[42] fabricated a $Ti_3C_2T_x$/SnO_2 composite *via* hydrothermal synthesis, achieving an exceptional specific capacity of 904 mA h g^{-1}. It shows that this synthetic technique is beneficial for energy storage applications. As a result, numerous strategies have been explored to improve the electrochemical performance of $Ti_3C_2T_x$, particularly targeting enhancement of its specific capacitance.

The $Ti_3C_2T_x$–SnO_2 NPs/PPy hybrid nanocomposite is electrochemically evaluated in this work as a hybrid capacitive electrode for electrochemical biosensing targeting the detection of *K. pneumoniae*. The formation mechanism of the $Ti_3C_2T_x$–

SnO_2 NPs nanocomposite involves several key steps, including the preparation of $Ti_3C_2T_x$, the synthesis or incorporation of SnO_2 NPs. For this, pre-synthesized SnO_2 NPs were dispersed with $Ti_3C_2T_x$ in a solvent (*e.g.*, ethanol/water) and sonicated to achieve homogeneity. The Sn–O–Ti covalent bonds were formed between SnO_2 NPs and oxygen-terminated $Ti_3C_2T_x$. Hydrogen bonding was formed between –OH groups on SnO_2 NPs and $Ti_3C_2T_x$, and $Ti_3C_2T_x$ acted as a support, inhibiting NPs agglomeration. $Ti_3C_2T_x$ provided high conductivity, while SnO_2 contributes to catalytic/adsorptive properties. Enhanced charge transfer (SnO_2 NPs → $Ti_3C_2T_x$) improves performance in applications, like energy storage, electrochemical biosensors. Therefore, $Ti_3C_2T_x$–SnO_2 NPs can enhance surface area for electrochemical sensing, and these properties can be further improved by integrating PPy functional materials.

In this study, $Ti_3C_2T_x$–SnO_2 NPs nanocomposites were synthesized and incorporated into PPy to fabricate an electrochemical capacitive electrode for biosensing applications. The electrochemical capacitive nature of $Ti_3C_2T_x$–SnO_2 NPs/PPy was characterized by cyclic voltammetry (CV), galvanostatic charge–discharge (GCD), electrochemical impedance spectroscopy (EIS), and Dunn methods. The results revealed that $Ti_3C_2T_x$–SnO_2 NPs/PPy exhibited a capacitive (supercapacitor) electrode type. The capacitive electrode ($Ti_3C_2T_x$–SnO_2 NPs/PPy) was modified with bacteriophage using charge-directed immobilization by applying a potential of +1.0 V for 10 minutes. Afterwards, the $Ti_3C_2T_x$–SnO_2 NPs/PPy/Phage electrode demonstrates effective infection and binding specificity toward the host *K. pneumoniae*. The bacterial-infected electrochemical response was measured *via* differential pulse voltammetry (DPV) and impedance-increasing EIS techniques. This is the first reported research on PPy functionalized capacitive electrode for electrochemical detection of *K. pneumoniae*, explaining the capacitive nature towards immobilization of bacteriophages. In this research, the developed hybrid capacitive electrode proved to be an efficient, selective, and cost-efficient sensor for quantifying *K. pneumoniae* to overcome the gap of conventional detection methods.

2 Reagents & methods

2.1. Chemicals

Materials were all analytical grades, and they were used as received with no extra purification. Ammonium persulfate (APS) (98%), pyrrole monomer (99.7%), and stannous chloride dihydrate ($SnCl_2 \cdot 2H_2O$) (99%) were obtained from Aladdin Reagent Co. (China). Ti_3AlC_2 MAX phase in powder form (particle size smaller than 0.04 nm) was obtained from Y-Carbon Ltd (Ukraine) as the Ti_3AlC_2 precursor, which was subsequently etched to produce $Ti_3C_2T_x$ following the previously reported protocol.[43] Potassium ferrocyanide ($K_4[Fe(CN)_6]$) (99.0%), potassium ferricyanide ($K_3[Fe(CN)_6]$)(99.0%), and potassium chloride (KCl) (99.5%) were purchased from Merck Life Science Pvt. Ltd Screen-printed carbon electrodes (SPEs, 3 mm diameter) were sourced from CH Instruments (Bee Cave, TX, USA). Type I-ultrapure deionized water (DI) with a resistance of 0.0182 Ω cm at room temperature was utilized for all solutions in this work. All glassware was thoroughly cleaned before use. *K. pneumoniae* was cultured by following the standard ATCC 700603. The SM buffer for bacteriophage storage was made by sodium chloride NaCl, magnesium sulfate ($MgSO_4$), and tris-hydrochloric acid (pH 7.5), and 10% gelatin (w/v) obtained from Aladdin Reagent Ltd (China). Furthermore, nutrient agar and Luria-Bertani were acquired from Oxoid (UK). 0.85% of NaCl was used to dilute the *K. pneumoniae*.

2.2. Instrumentation and characterization

The topology of the $Ti_3C_2T_x$ flakes, SnO_2 NPs, and $Ti_3C_2T_x$–SnO_2 NPs/PPy nanocomposite modified electrode was examined employing a scanning electron microscope (SEM, ZEISS Gemini SEM 500, UK) operated at 15 kV of accelerating voltage. The crystalline phases of $Ti_3C_2T_x$ were analyzed with an X-ray diffractometer (D/teX Ultra2, EMPYREAN, PANalytical, Netherlands), using Cu Kα radiation ($\lambda = 154\ 10^{-3}$ μm) over a 2θ range of 10°–95° at a scan rate of 2° min^{-1} with texture mode. The working distance was maintained between 10.0 and 11.1 mm, and the emission current ranged from 9000 to 10 100 nA. EIS, CV, and DPV measurements were conducted utilizing two electrochemical workstations: Corrtest CS350 (China) and AUT 53154 (Metrohm, Switzerland). Attenuated total reflectance Fourier transform infrared spectroscopy (ATR-FTIR, PerkinElmer, Waltham, MA, USA) was employed to analytically characterize the structure of the synthesized materials. EIS analysis was conducted across a frequency range from 0.1 MHz to 0.1 Hz in 0.1 mol per L KCl containing 0.005 mol per L $[Fe(CN)_6]^{3-/4-}$ to evaluate the resistivity. For the electrochemical detection of *Klebsiella pneumoniae*, all media, buffers, and glassware were thoroughly sterilized before their use with both *K. pneumoniae* and its corresponding bacteriophage.

2.3. Fabrication of $Ti_3C_2T_x$–SnO_2 NPs/PPy nanocomposite

SnO_2 NPs were fabricated *via* a modified, template-free hydrothermal method, adapted from previously reported protocols.[44–46] In a typical procedure, 800 mg of stannous chloride dihydrate ($SnCl_2 \cdot 2H_2O$) was dissolved in a solvent mixture of 0.04 L of ethanol and 80 mL of DI. The solution was mixed continuously and heated to 50 °C for 60 minutes. The resultant mixture was transferred to a Teflon-lined stainless-steel autoclave and was exposed to hydrothermal treatment at 180 °C for 8 hours. The white precipitate was collected by centrifugation, washed repeatedly with DI and ethanol, and vacuum-dried at 50 °C for 48 hours. For enhancing their electrochemical properties, the dried SnO_2 nanoparticles (SnO_2 NPs) underwent calcination in air at 600 °C for 3 hours, with a controlled heating rate of 10 °C per minute.

The as-prepared SnO_2 NPs were ultrasonically dispersed with $Ti_3C_2T_x$ for 45 minutes, followed by mixing for 30 minutes to form the $Ti_3C_2T_x$–SnO_2 NPs nanocomposite. The synthesis of PPy was carried out based on previously reported procedures.[47–49] Specifically, 1.369 g (60 mM) of APS was dissolved in 0.1 L of DI, and 210.2 μL (0.03 M) of pyrrole monomer was added while maintaining the reaction temperature at 10 °C to obtain a black suspension. The solution was mixed for 8

Scheme 1 Graphic representation of the preparation of PPy and $Ti_3C_2T_x$–SnO_2 NPs powder for SPE/$Ti_3C_2T_x$–SnO_2 NPs/PPy fabrication.

hours to guarantee complete polymerization. The resulting PPy product was collected by filtration and purified using a Soxhlet extractor with water and ethanol to eliminate residual oxidant. Then, a vacuum oven set at 60 °C for 12 hours was used to dry the purified PPy powder. A graphic illustration of the fabrication and surface decoration strategy for the $Ti_3C_2T_x$–SnO_2 NPs/PPy nanocomposite is presented in Scheme 1. For the modification of the SPE, the $Ti_3C_2T_x$–SnO_2 NPs/PPy nanocomposite was deposited onto the electrode surface using a drop-casting technique. First, the $Ti_3C_2T_x$–SnO_2 NPs nanocomposite was dissolved in *N*,*N*-dimethylformamide and dropped-cast onto the SPE. Subsequently, PPy was dispersed in *N*,*N*-dimethylformamide, dropped-casted onto the SPE/$Ti_3C_2T_x$–SnO_2 NPs, and vacuum dried at 60 °C and stored for further usage.

2.4. Pneumoniae and phage preparation

2.4.1. Revival and preparation of *K. pneumoniae*. *K. pneumoniae* ATCC 700603, a well-characterized reference strain known for its sensitivity to meropenem, as reported in previous studies[50] was employed in this investigation. The strain was provided by the Department of Microbiology at Jashore University of Science and Technology. To revive the strain, 100 μL of glycerol stock was inoculated into 5×10^3 μL of trypticase soy broth under standard conditions. Following enrichment, the culture was streaked onto MacConkey agar plates and incubated at 37 °C overnight to isolate individual colonies. Morphologically distinct colonies were examined microscopically and subjected to a series of standard biochemical tests to confirm their identity as *K. pneumoniae* before their use in downstream experiments. *K. pneumoniae* was isolated from hospital effluent water collected near a river in Jashore city, Bangladesh. For the isolation process, 10 mL of filtered effluent sample was inoculated into 0.9 L of Mueller–Hinton broth and incubated at 37 °C overnight. Following incubation, the enriched culture was spread onto MacConkey selective agar to allow colony formation. Individual colonies were then purified and subjected to microscopic examination and standard biochemical tests. Presumptive *K. pneumoniae* isolates, intended as host bacteria for bacteriophage studies, were further cultured in Mueller–Hinton broth and subsequently placed on Mueller–Hinton agar to obtain pure cultures. Biochemical characterization, along with SI data from a previously published study, confirmed that the isolated strain is identical to *Klebsiella pneumoniae* ATCC 700603.[50]

2.4.2. Phage isolation and purification. For phage isolation, several sewage samples were gathered from hospital effluents. The samples were first centrifuged at 10^4 rpm for 15 minutes. The supernatant was then sieved through a 220 nm syringe filter to isolate bacteriophages potentially targeting unknown bacterial hosts. For phage enrichment, 0.005 L of the filtered bacteriophage-containing solution was mixed with 10 mL of Luria–Bertani (LB) broth and inoculated with *K. pneumoniae* strain ATCC 700603. The solution was incubated for 24 hours at 37 °C with gentle shaking. Next, the culture was centrifuged for 15 minutes to lyse the bacterial cells, and the supernatant was again sieved using a 220 nm syringe filter to purify the bacteriophages. To enhance selectivity and purity, this infection, centrifugation, and filtration cycle was repeated ten times using fresh *K. pneumoniae* cultures. The presence of lytic bacteriophages was confirmed *via* spot tests, which involved spotting phage suspensions onto bacterial lawns and incubating overnight at 37 °C until zones of clearance were observed. Each phage isolate was subjected to five successive rounds of single plaque purification to obtain clonal bacteriophages. Then, the Bacteriophage titer was determined using the double-layer agar plate technique. Serial dilutions of the phage suspensions were prepared in SM buffer for accurate quantification. Furthermore, the host range and spot test were performed.

2.5. Electrode preparation and *K. pneumoniae* detection

The SPE was first activated *via* electrochemical pre-anodization in 1.0 M H_2SO_4 solution at +1.5 V for 15 minutes. Next, the electrode was ultrasonicated in DI for 5 minutes and then dried under a nitrogen stream. For surface modification, 5.0 μL of a freshly prepared homogeneous suspension of $Ti_3C_2T_x$–SnO_2 NPs nanocomposite was drop-casted onto the SPE and dried at 60 °C in a vacuum oven. Then, the second drop-casting step was

performed using a PPy dispersion to complete the composite layering. The total amount of deposited electrode material was determined by direct weighing. The resulting SPE/$Ti_3C_2T_x$–SnO_2 NPs/PPy electrode was employed directly for supercapacitor characterization and subsequently functionalized with bacteriophages for biosensor applications. For phage immobilization, 5.0 μL of bacteriophage solution (10^8 PFU mL^{-1} in PBS) was drop-casted onto the electrode and immobilized anodically at +1.0 V for 15 minutes using a chronoamperometric method. After immobilization, the electrode was washed with PBS to get rid of unbound phages. To perform bacterial detection, the biosensor was incubated in a solution containing *K. pneumoniae* for 30 minutes, allowing sufficient interaction between the immobilized phages and the target bacteria. The electrode was then washed out again with PBS to eliminate nonspecifically adhered bacterial cells. Finally, electrochemical signals of the SPE/$Ti_3C_2T_x$–SnO_2 NPs/PPy/Phage/*K. pneumoniae* biosensor were measured in a $[Fe(CN)_6]^{3-/4-}$ redox probe solution utilizing DPV and EIS.

3 Results and discussion

3.1. Analytical characterization: FTIR & XRD investigation

Fig. 1 shows the ATR-FTIR spectra of $Ti_3C_2T_x$, SnO_2 NPs, $Ti_3C_2T_x$–SnO_2 NPs, PPy, and $Ti_3C_2T_x$–SnO_2 NPs/PPy. In the spectrum, the absorption bands at 1130, 822, and 505 cm^{-1} correspond to C–O, C–F, and Ti–O stretching vibrations.[51] The C–F and Ti–O were confirmed by following the etching and exfoliation procedure, and they matched with previously published research.[43] The spectrum of the annealed SnO_2 NPs shows peaks at about 505 and 605 cm^{-1}, showing the vibrations connected to Sn–O bonds.[52] For $Ti_3C_2T_x$–SnO_2 NPs, the peaks around 609 cm^{-1} and 487 cm^{-1} are for the vibration of Sn–O and Ti–O bonds, respectively, confirming the presence of $Ti_3C_2T_x$ and SnO_2 NPs. During analysis of PPy spectrum, the peaks at 1689, 1552, and 1471 cm^{-1} are attributed to stretching vibration of the pyrrole ring (C=H, C–N). Additionally, those at 1296 cm^{-1} and 1042 cm^{-1} are due to the in-plane vibrations of C–H.[53,54] The sharp peak observed at 1181 cm^{-1} is because of the C–N stretching vibrations, and 1042 cm^{-1} is for the in-plane deformation vibration.[54] The peak appearing at 901 cm^{-1} relates to the C–C deformation vibrations, and the peaks at 788 cm^{-1} and 675 cm^{-1} are due to the aromatic ring bending vibrations.[55] Furthermore, PPy in $Ti_3C_2T_x$–SnO_2 NPs shows the symmetric peaks for PPy. However, all peaks are slightly shifted to the left side with increasing wavenumber. These shifts provide insight into interfacial bonding, the electronic environment, or structural reorganization, thereby confirming the successful formation of a composite. FTIR spectroscopy is a powerful tool for detecting such interactions, as it reveals changes in the vibrational environment of functional groups. Shifts in stretching frequencies, for example, in –OH, –NH, or –C=O groups, may signify hydrogen bonding or covalent interactions between the matrix and the filler.[56] Additionally, the appearance or disappearance of specific peaks can indicate new chemical bonding or functionalization events during composite formation. For instance, a redshift (shift to a lower wavenumber) in the –OH stretching band is typically associated with hydrogen bonding between polymer chains and nanoparticles, providing direct evidence of interfacial interaction.[57]

The XRD patterns of Ti_3AlC_2, $Ti_3C_2T_x$, SnO_2 NPs, $Ti_3C_2T_x$–SnO_2 NPs, and $Ti_3C_2T_x$–SnO_2 NPs/PPy are shown in Fig. 1(B). The peaks of Ti_3AlC_2 at 2θ values of 9.54°, 19.1°, 34.04°, 38.86°, 41.8°, 48.38°, 56.32°, 60.02°, 70.18°, and 73.86° are assigned to the (002), (004), (004), (104), (105), (107), (109), (110), (112), (118), respectively, according to JCPDS no. 520875.[58] The crystallinity and structural order of Ti_3AlC_2 changed by disappearing the Al layers at 38.86° with HF etching for $Ti_3C_2T_x$ synthesis.[43] In $Ti_3C_2T_x$, the (002) peak is displaced to 5.46° for the removal of Al atoms. This peak shift is a well-established fingerprint of the successful Al layer removal and the formation of few-layered or delaminated $Ti_3C_2T_x$, often indicating

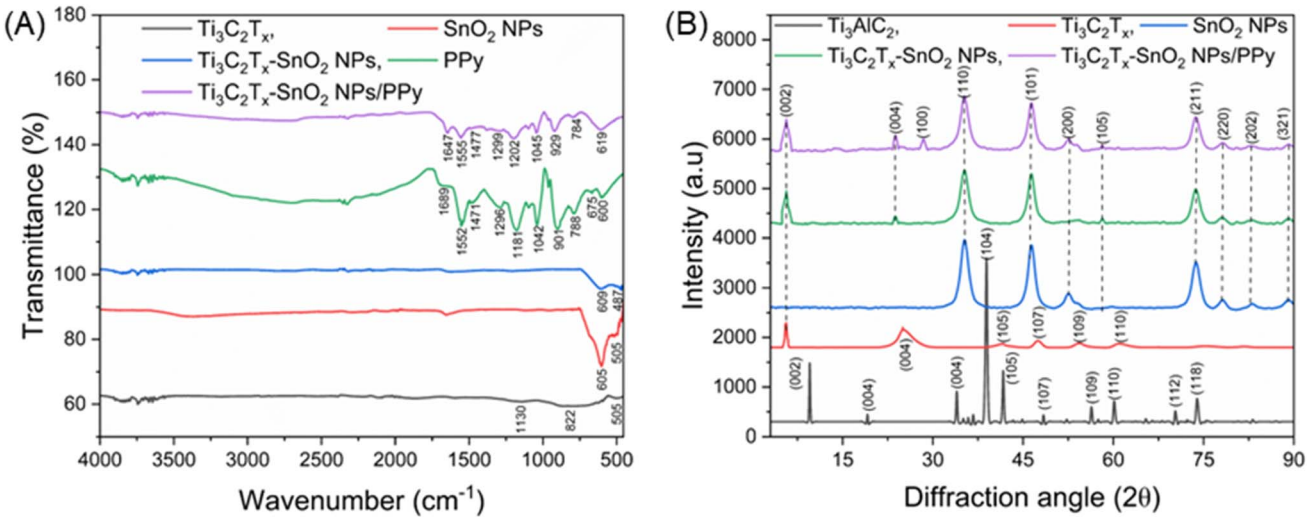

Fig. 1 (A) ATR-FTIR of as-prepared (i) $Ti_3C_2T_x$, (ii) SnO_2 NPs, (iii) $Ti_3C_2T_x$–SnO_2 NPs, (iv) PPy, (v) $Ti_3C_2T_x$–SnO_2 NPs/PPy, (B) XRD of (i) Ti_3AlC_2, (ii) $Ti_3C_2T_x$, (iii) SnO_2 NPs, (iv) $Ti_3C_2T_x$–SnO_2 NPs, (v) $Ti_3C_2T_x$–SnO_2 NPs/PPy.

increased interlayer spacing due to surface functionalization or intercalation. The XRD results of as-fabricated SnO_2 NPs shown in Fig. 1(B), display the diffraction patterns peaks at (110), (101), (200), (105), (211), (220), (202), and (321) at 2θ diffraction angles of 35.16°, 46.4°, 52.44°, 58.04°, 73.7°, 78.22°, 83.68°, and 89.22°, consecutively. These peaks are found in the tetragonal rutile structure of the cassiterite crystal phase (JCPDS no. 41-1445).[59,60] In the $Ti_3C_2T_x$–SnO_2 NPs spectrum, both $Ti_3C_2T_x$ and SnO_2 NPs individually show the peak of diffraction planes; however, $Ti_3C_2T_x$ peaks overlap with SnO_2 NPs. The diffraction planes of the peaks of (002), (004), (110), (101), (200), (105), (211), (220), (202), and (321) are displayed in $Ti_3C_2T_x$–SnO_2 NPs, which confirms the successful mixing of $Ti_3C_2T_x$–SnO_2 NPs nanocomposite. Eventually, the XRD pattern of $Ti_3C_2T_x$–SnO_2 NPs/PPy indicates the reflection plane of $Ti_3C_2T_x$–SnO_2 NPs with a new (100) plane. The peaks at (100) with 2θ diffraction angle indicate the presence of PPy in $Ti_3C_2T_x$–SnO_2 NPs/PPy. This analysis supports the results obtained from the FTIR analysis, indicating the successful formation of a composite among $Ti_3C_2T_x$, SnO_2 NPs, and PPy.

3.2. Morphological investigations

Field Emission Scanning Electron Microscopy (FE-SEM), Energy-Dispersive X-ray Spectroscopy (EDX), and elemental mapping were utilized to characterize the topology and elemental analysis of the modified electrode. The FE-SEM images were collected from hydrothermally synthesized SnO_2 NPs with a 100 nm scale, as shown in Fig. 2(A). The nanoparticle is nanosphere-like, and the diameter was found to be 24.97 nm, from the average of five particle sizes. The FE-SEM image supports the FT-IR and XRD results of SnO_2 NPs. Fig. 2(B) displays the microscopic image of PPy nanoparticles, which are around five times greater than the particle size of SnO_2 NPs. The FE-SEM images are like previously reported research work.[61–63] Fig. 2(C) displays a FE-SEM picture of multilayered, crystalline $Ti_3C_2T_x$. As demonstrated in previously reported work, each flake has a thickness of around 1.25 nm and a hexagonal structure.[43] Fig. 2(D) displays the FE-SEM image of $Ti_3C_2T_x$–SnO_2 NPs nanostructure, confirming the insertion of SnO_2 NPs in $Ti_3C_2T_x$, and increasing the porosity and surface area. The FT-IR and XRD results, along with recently published research, support the formation and electrochemical applications of $Ti_3C_2T_x$–SnO_2 NPs nanocomposite.[64,65] In Fig. 2(E), the FE-SEM image of $Ti_3C_2T_x$–SnO_2 NPs/PPy is presented, in which PPy is covered on the $Ti_3C_2T_x$–SnO_2 NPs nanostructure. The homogeneous dispersion of PPy confirms the successful attachment to the $Ti_3C_2T_x$–SnO_2 NPs structure. The SEM images in Fig. 2(A–E) demonstrate a progressive increase in surface porosity, attributed first to the incorporation of SnO_2 NPs into $Ti_3C_2T_x$, as evident in Fig. 2(D), and further enhanced by the subsequent drop-casting of circular PPy structures, as illustrated in Fig. 2(E). Therefore, this modification strategy led to the successive increase of active surface area.

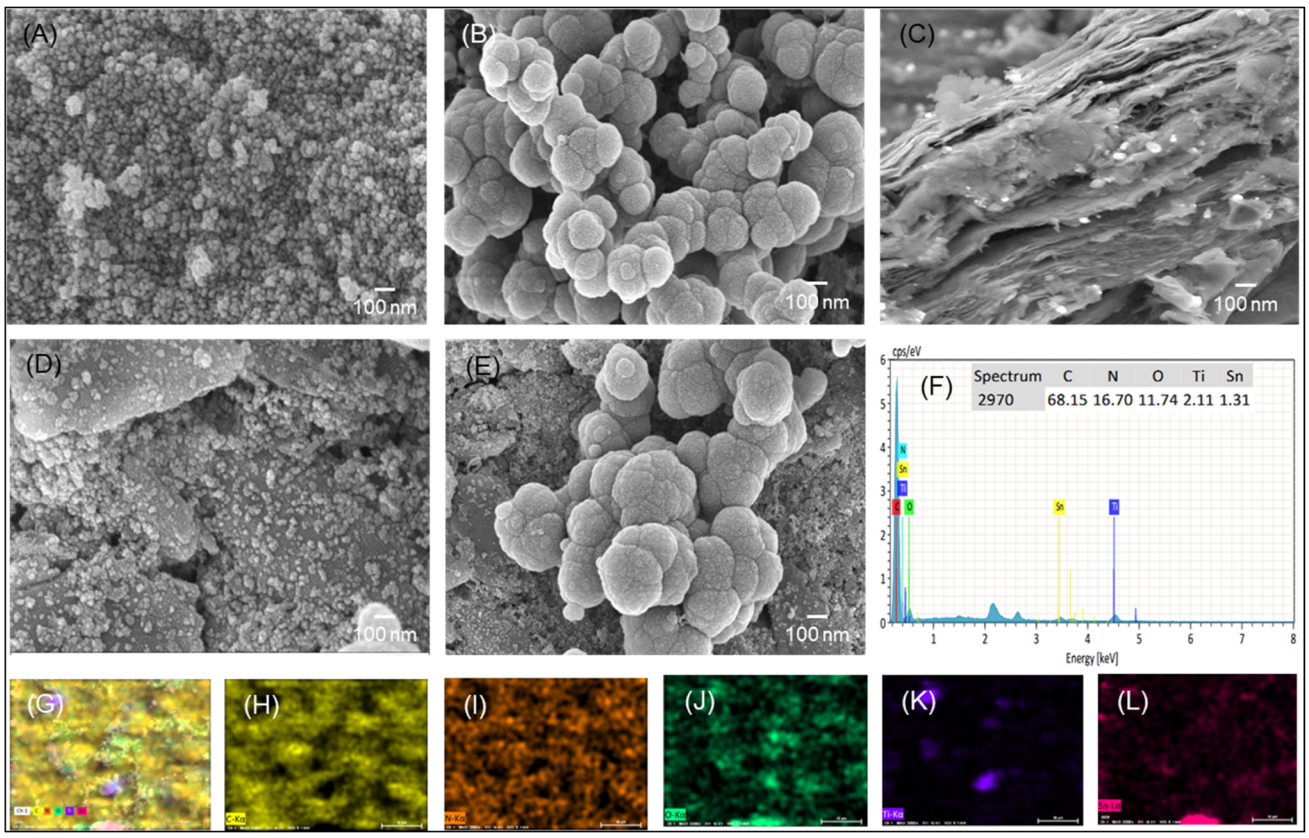

Fig. 2 FE-SEM images of (A) SnO_2 NPs, (B) PPy, (C) $Ti_3C_2T_x$, (D) $Ti_3C_2T_x$–SnO_2 NPs, (E) $Ti_3C_2T_x$–SnO_2 NPs/PPy, (F) EDX of $Ti_3C_2T_x$–SnO_2 NPs/PPy, (G) elemental mapping of $Ti_3C_2T_x$–SnO_2 NPs/PPy, (H) carbon map, (I) nitrogen map, (J) oxygen map, (K) titanium map, and (L) tin map.

The $Ti_3C_2T_x$–SnO_2 NPs/PPy modified electrode consists of 68.15% of C, 11.74% of O, 2.11% of Ti, and 16.70% of N, as shown in the EDX results represented in Fig. 2(F), indicating the C, O, Ti elements from $Ti_3C_2T_x$ and N from PPy. Furthermore, Fig. 2(G–L) display the elemental mapping of $Ti_3C_2T_x$–SnO_2 NPs/PPy, where the C, N, O, Ti, and N are visually represented by distinct colors shown in Fig. 2(H–L). Therefore, the element shown in the EDX spectra was identified by elemental mapping.

3.3. $Ti_3C_2T_x$–SnO_2 NPs/PPy for electrochemical biosensing

In the phage-based biosensor, bacteriophage was attached to the $Ti_3C_2T_x$–SnO_2 NPs/PPy modified according to potential-driven chronoamperometry techniques, where the current follows a constant concerning time (s) and potential (V), as presented in Fig. 3(A and B). As the current remains constant around 1.0 V, the immobilization process feels like charging, as displayed in Fig. 3(C). As phage immobilization is a charging phenomenon, the charge holding time analysis is important. The charge retaining capability was studied utilizing the self-discharging data presented in Fig. 3(D–G) of $Ti_3C_2T_x$–SnO_2 NPs/PPy electrode in H_2SO_4. The H_2SO_4 electrolyte is an alternative to phage, where H_2SO_4 is mostly utilized as an ionic medium to explain the capacitive behavior of the electrode material.[66] While a well-capacitive surface can support bacteriophage immobilization, the instability of bacteriophages, particularly at room temperature, poses a significant challenge for long-term capacitive measurements in phage-based biosensors. Careful consideration of phage stability and the implementation of appropriate preservation strategies are crucial for developing reliable phage-based capacitive biosensors.

Moreover, the stability of the bacteriophages under varying temperature and pH conditions is illustrated in Fig. S1(A and B)

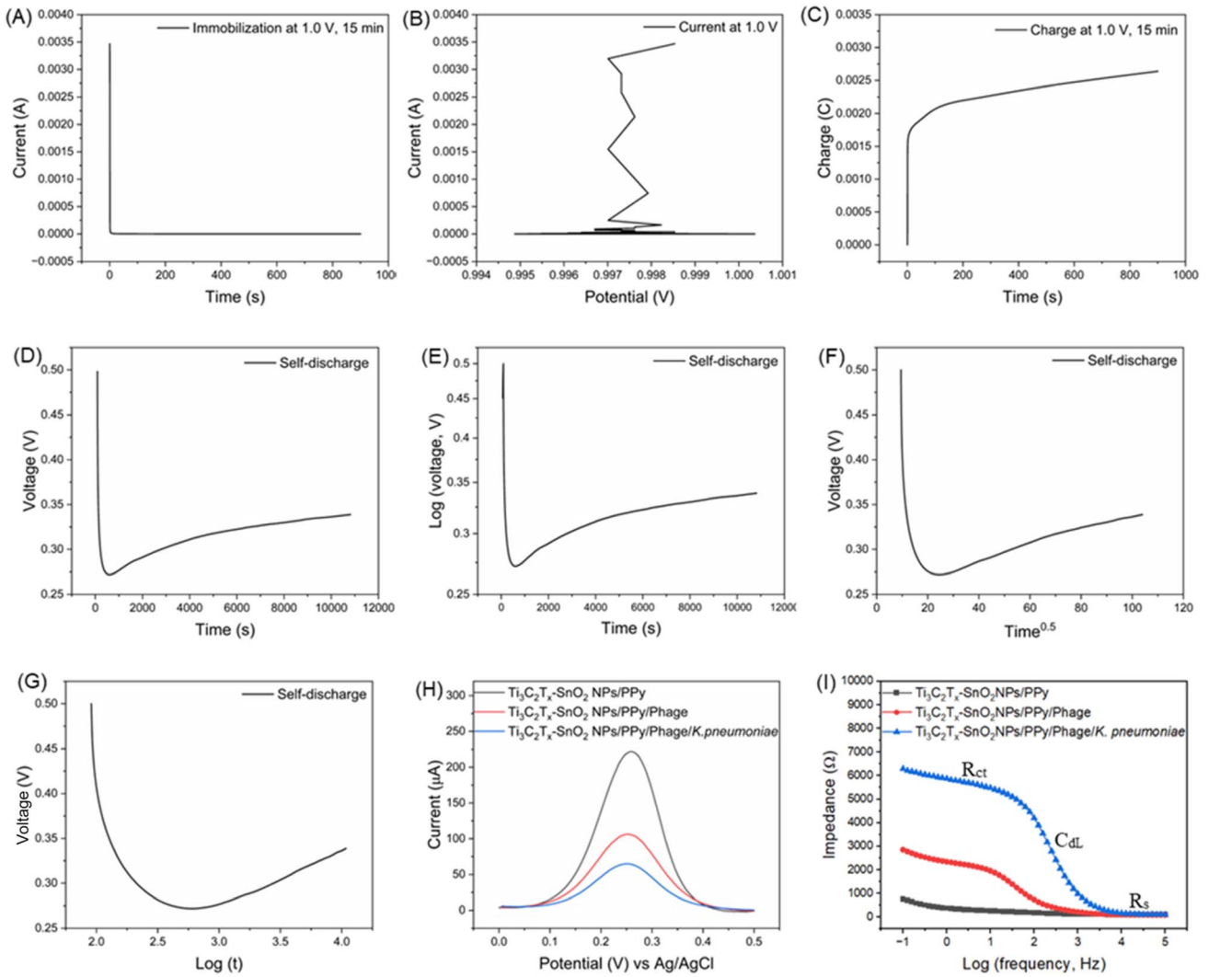

Fig. 3 (A) Potentiostatic (chronoamperometry) immobilization of bacteriophage, (B) corresponding current of potentiostatic immobilization at 1.0 V, (C) corresponding charge during potentiostatic immobilization, (D) self-discharge plot of $Ti_3C_2T_x$–SnO_2 NPs/PPy electrode in H_2SO_4 after charging (2.0 Ag^{-1} up to 0.5 V), and corresponding plot of (E) log(potential) *versus* time of self-discharge, (F) potential *vs.* time$^{0.5}$, (G) voltage *versus* log(time), (H) DPV response, (I) Bode plot of showing $Ti_3C_2T_x$–SnO_2 NPs/PPy, after immobilization of bacteriophage, and attacking of *K. pneumoniae*.

of the SI. At temperature values of −20, 4, 25, and 37 °C, the concentration of bacteriophage remains constant but decreases at over 56, 70, and 100 °C. Also, the bacteriophage was stable at an optimum pH of 7.0 without destroying any plaques but decreases at lower and higher pH levels of 4.0 and 10.0. To assess the self-discharge behavior of the $Ti_3C_2T_x$–SnO_2 NPs/PPy modified electrode, it was initially charged up to 0.5 V with a 2 A g^{-1} of current density. The corresponding self-discharge profile is presented in Fig. 3(D). The electrode exhibited a minor voltage drop during the early stage of the self-discharge activity, followed by a stable stage where no significant voltage loss was observed, indicating excellent charge retention. The self-discharge mechanism was interpreted based on methodologies previously reported.[67] The self-discharge of capacitive or supercapacitor electrodes can be attributed to three primary factors: (i) diffusion-controlled redox reactions, (ii) overcharging beyond the optimal voltage window, and (iii) ohmic leakage through the internal resistance of the device.[68] Fig. 3(E) presents the plot of the logarithm of (V) *vs.* time (t), displaying a consistent linear relationship indicative of a diffusion-controlled self-discharge process, with no evidence of ohmic leakage in the $Ti_3C_2T_x$–SnO_2 NPs/PPy modified electrode.[69] The plot of voltage (V) *vs.* $t^{0.5}$ shown in Fig. 3(F) demonstrates linearity in the steady-state region, indicating the predominance of capacitive-controlled processes and the absence of ohmic leakage during self-discharge. Moreover, the linear profile observed in the V *versus* log(t) plot confirms that the self-discharge of the $Ti_3C_2T_x$–SnO_2 NPs/PPy modified electrode is not governed by overcharging-induced charge redistribution.[70]

A comparative oxidation peak of $Ti_3C_2T_x$–SnO_2 NPs/PPy, $Ti_3C_2T_x$–SnO_2 NPs/PPy/Phage, and $Ti_3C_2T_x$–SnO_2 NPs/PPy/Phage/*K. pneumoniae* was collected in 100 mmol per L KCl containing 5 mmol L^{-1} of $[Fe(CN)_6]^{3-/4-}$. From the DPV study, the oxidation current was found to be 218.27 μA for SPE/$Ti_3C_2T_x$–SnO_2 NPs/PPy, 102.73 μA for SPE/$Ti_3C_2T_x$–SnO_2 NPs/PPy/Phage, and 61.11 μA for SPE/$Ti_3C_2T_x$–SnO_2 NPs/PPy/Phage/*K. pneumoniae*. The oxidation current gradually decreased from the developed SPE/$Ti_3C_2T_x$–SnO_2 NPs/PPy modified electrode due to the successful immobilization of phage and hosting *K. pneumoniae* on the immobilized phage. Furthermore, impedance-based EIS data were collected for $Ti_3C_2T_x$–SnO_2 NPs/PPy, $Ti_3C_2T_x$–SnO_2 NPs/PPy/Phage, and $Ti_3C_2T_x$–SnO_2 NPs/PPy/Phage/*K. pneumoniae* functionalized electrodes, and the Bode plot is displayed in Fig. 3(I). Bode plot reveled that the charge transfer resistance (R_{ct}) was determined to be 200 Ω for SPE/$Ti_3C_2T_x$–SnO_2 NPs/PPy, 3424 Ω for $Ti_3C_2T_x$–SnO_2 NPs/PPy/Phage, and 6260 Ω for $Ti_3C_2T_x$–SnO_2 NPs/PPy/Phage/*K. pneumoniae*. The R_{ct} value gradually increased from the developed SPE/$Ti_3C_2T_x$–SnO_2 NPs/PPy due to immobilization of Phage and hosting *K. pneumoniae* on immobilized bacteriophage, confirming the presence of capacitive double layer (C_{dL}). Therefore, bacteriophage immobilization and *K. pneumoniae* hosting are certainly capacitive phenomena. The corresponding Nyquist plot of Fig. 3(I) is shown in Fig. S1(C). The phage and *K. pneumoniae* can successfully decrease the DPV current and increase the value of R_{ct}. So, the DPV and EIS results assured the successful immobilization of bacteriophage onto the surface of the $Ti_3C_2T_x$–SnO_2 NPs/PPy modified electrode after hosting the targeted *K. pneumoniae* ATCC 700603. Also, the attacking ability of the isolates of bacteriophage to *K. pneumoniae* ATCC 700603 and the hospital effluent collected *K. pneumoniae* is presented in Fig. S2(A and B). The host range testing results towards *Salmonella typhi* (*S. typhi*), *E. coli* DH5α, *E. coli* 0157:H7, *Pseudomonas aeruginosa* (*P. aeruginosa*), *Shigella flexneri* (*S. flexneri*), *Vibrio cholerae* (*V. cholera*), *Salmonella enterica* (*S. enterica*), and *Listeria monocytogenes* (*L. monocytogenes*) are selective as shown in Fig. S2(C–J). This study confirms that the *K. pneumoniae* ATCC 700603 strain and the collected *K. pneumoniae* are identical.

3.4. Electrode characterization through supercapacitor studies

The power law equation controlling the correlation between peak current and scan rate is considered to comprehend the charge storage mechanism, as shown in eqn (1). The correlation between the logarithm of scan rate and the logarithm of peak current is presented in Fig. 4(A). Here, the slope is used to determine the b value.[68] In general, a b-value between 0.5 and 1 suggests a combination of diffusion-controlled and surface-controlled (pseudocapacitive) charge storage. A b-value closer to 0.5 indicates that diffusion-controlled processes dominate, while a value closer to 1 implies that capacitive behavior is more dominant. For PPy, $Ti_3C_2T_x$–PPy, $Ti_3C_2T_x$–SnO_2 NPs, and $Ti_3C_2T_x$–SnO_2 NPs/PPy, the b value is 0.656, 0.456, 0.962, and 0.830, respectively, in which $Ti_3C_2T_x$–SnO_2 NPs show the highest b-value, and the b value for PPy increased from 0.656 to 0.830 in $Ti_3C_2T_x$–SnO_2 NPs/PPy. The results show that the hybrid electrode has both surface and diffusion processes. Furthermore, diffusion-controlled charge storage and surface capacitance are estimated using the widely recognized Dunn method, as outlined in eqn (3) and (4). In this case, $I(V)$, $k_2v^{1/2}$ and k_1v stands for the total current at a given voltage, the diffusion contribution, and the surface control contribution, respectively. Fig. 4(B) represents the capacitive and surface-controlled contribution (%) plot of $Ti_3C_2T_x$–SnO_2 NPs/PPy. Based on eqn (4), the plot of $I(V)/v^{1/2}$ *versus* $k_1v^{1/2}$ for $Ti_3C_2T_x$–SnO_2 NPs/PPy was used to calculate the constant k_1 and k_2 at the potential of 0.335 V for the anodic sweep, with the scan rate varying from 10 to 60 mV s^{-1}. At a scan rate of 5 mV s^{-1}, the surface control contribution is 90% and reaches 96% at 60 mV s^{-1}. This is because there is not enough time for a diffusion layer to develop at a fast scan rate.

$$I = av^b \quad (1)$$

$$\log I = \log a + b \log v \quad (2)$$

$$I(V) = k_1v + k_2v^{1/2} \quad (3)$$

$$I(V)/v^{1/2} = k_1v^{1/2} + k_2 \quad (4)$$

To evaluate the electrochemical properties of the sythasized materials, PPy, $Ti_3C_2T_x$–PPy, $Ti_3C_2T_x$–SnO_2 NPs, and $Ti_3C_2T_x$–

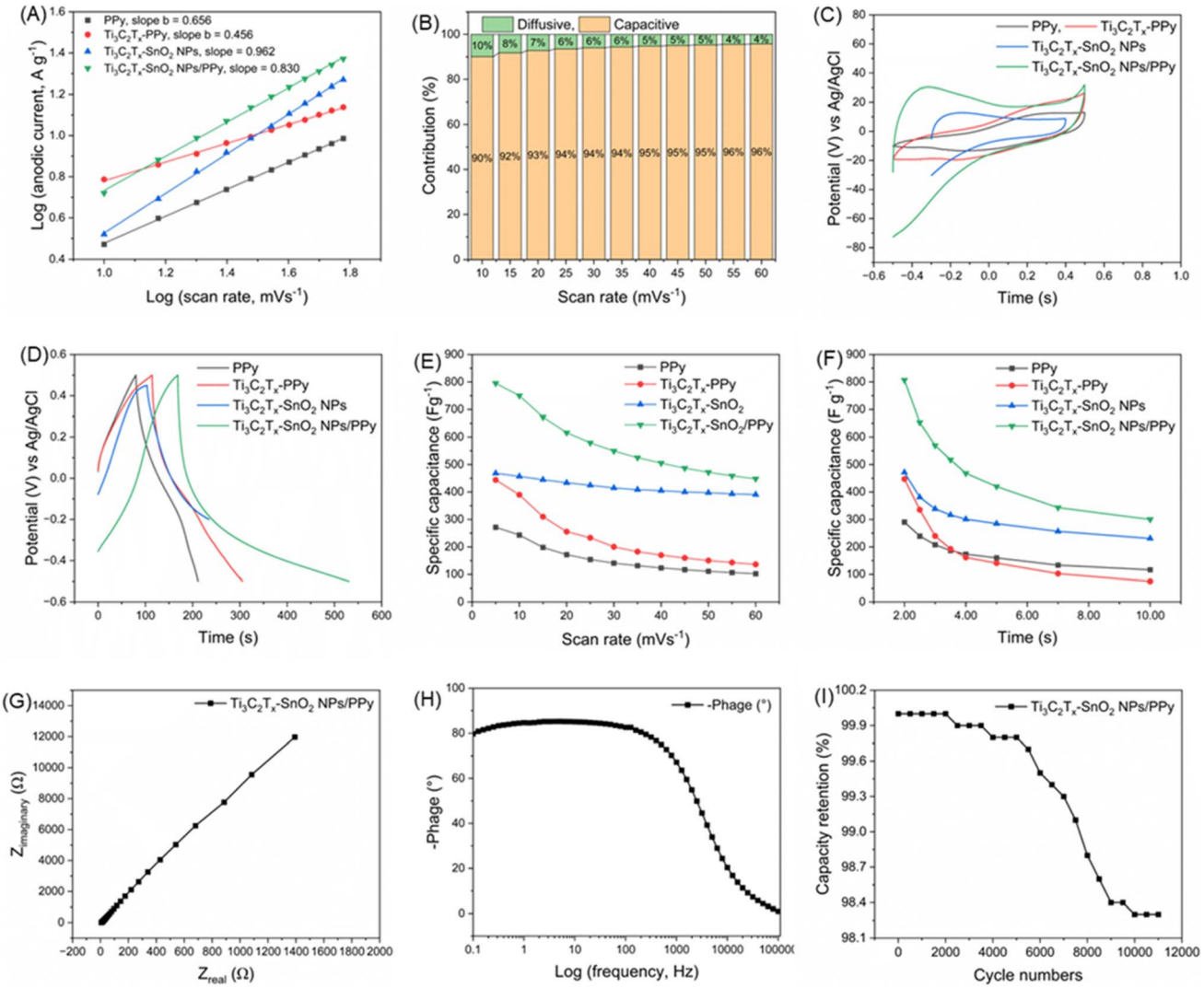

Fig. 4 In 1.0 mol per L H_2SO_4 solution, (A) determination of *b* value of $Ti_3C_2T_x$–SnO_2 NPs/PPy and sub electrodes, (B) contribution (%) of capacitive controlled and diffusion controlled charge storage processes of $Ti_3C_2T_x$–SnO_2 NPs/PPy (C) CV and (D) GCD comparison profile of PPy, $Ti_3C_2T_x$–PPy, $Ti_3C_2T_x$–SnO_2 NPs, and $Ti_3C_2T_x$–SnO_2 NPs/PPy, (E) comparison of corresponding specific capacitance of CV and (F) GCD, (G) Nyquist and (H) Bode plot of $Ti_3C_2T_x$–SnO_2 NPs/PPy, (I) GCD stability at the charging–discharging current density of 4.0 A g^{-1} over 10 000 cycles.

SnO_2 NPs/PPy, CV and GCD measurements were conducted using a 3-electrode setup, with 1 mol per L H_2SO_4 as the aqueous electrolyte. Fig. 4(C) presents a comparison of the CV curves. They were recorded at a scan rate of 50 mV s^{-1}, with voltage range of −0.3–0.4 V for $Ti_3C_2T_x$–SnO_2 NPs, and −0.5–0.5 V for PPy, $Ti_3C_2T_x$–PPy, $Ti_3C_2T_x$–SnO_2 NPs/PPy (*vs.* Ag/AgCl). The recorded rectangular CV curves indicate ideal capacitive behavior with current response proportional to scan rate and independent of the potential. However, these rectangular shapes can be distorted by various factors, including faradaic reactions and pseudocapacitive behavior.[69] The CV curve also indicates that current changes instantaneously with voltage changes, with constant capacitance within the voltage range.

The $Ti_3C_2T_x$–SnO_2 NPs/PPy modified electrode showed an oxidation peak at a voltage of 0.335 V, indicating Faradaic behavior of pseudocapacitance electrode. Furthermore, the CV curve has a rectangular shape, thus, $Ti_3C_2T_x$–SnO_2 NPs/PPy is a pseudocapacitance-type supercapacitor electrode. The CV results for PPy, $Ti_3C_2T_x$–PPy, $Ti_3C_2T_x$–SnO_2 NPs, and $Ti_3C_2T_x$–SnO_2 NPs/PPy are shown in Fig. S(3). Furthermore, the GCD comparison profile of PPy, $Ti_3C_2T_x$–PPy, $Ti_3C_2T_x$–SnO_2 NPs, and $Ti_3C_2T_x$–SnO_2 NPs/PPy, is displayed in Fig. 4(D), and the detailed GCD curves are presented in Fig. S(4). From the GCD curves, it was observed that a rectangular shape was obtained with no IR drop. Therefore, the CV and GCD revealed that $Ti_3C_2T_x$–SnO_2 NPs/PPy is a supercapacitor-type electrode. The CV specific capacitance comparison is shown in Fig. 4(E), where $Ti_3C_2T_x$–SnO_2 NPs/PPy show higher than PPy, $Ti_3C_2T_x$–PPy, and $Ti_3C_2T_x$–SnO_2 NPs, which was calculated from eqn (5). The specific capacitance of $Ti_3C_2T_x$–SnO_2 NPs/PPy was found to be 795.0 F g^{-1}, 271.85 F g^{-1}, 444.0, and 468 F g^{-1} for PPy, $Ti_3C_2T_x$–PPy, $Ti_3C_2T_x$–SnO_2 NPs at a scan rate of 0.005 V s^{-1}. Similarly, the specific capacitance of the GCD curve is shown in Fig. 4(F) and was calculated using eqn (6). The PPy, $Ti_3C_2T_x$–PPy, $Ti_3C_2T_x$–SnO_2 NPs, and $Ti_3C_2T_x$–SnO_2 NPs/PPy, nanocomposites

Table 1 Supercapacitor performance comparison of this work with previously published $Ti_3C_2T_x$/PPy-based electrodes

Electrode material	Synthesis method of PPy	Specific capacitance F g^{-1}	Current density or scan rate	Potential range (V)	Electrolyte	Capacitance retention (%)	Ref.
$Ti_3C_2T_x$/PPy	Chemical oxidation	416	5 mV s^{-1}	−0.2–0.35	H_2SO_4	92% over 25 × 10^3 cycles	71
$Ti_3C_2T_x$/PPy-PVA	Chemical oxidation	614	1 A g^{-1}	−0.5–0.6	H_2SO_4	100% over 10^3 cycles	72
$Ti_3C_2T_x$@PPY NW	Chemical oxidation	610	25 A g^{-1}	0–0.6	KOH	100% over 14 000 cycles	73
$Ti_3C_2T_x$/PPy	Chemical oxidation	437	5 mV s^{-1}	−0.8–0.2	H_2SO_4	76% 10^3 cycles	74
$Ti_3C_2T_x$/PPy@Cotton	Chemical oxidation	506.6	1 A g^{-1}	0–0.5	H_2SO_4	83.3% over 2000 cycles	75
$Ti_3C_2T_x$–SnO_2	Chemical oxidation	471.32	2.0 A g^{-1}	−0.3–0.4	H_2SO_4	N/A	This work
$Ti_3C_2T_x$/PPy	Chemical oxidation	448.4	2.0 A g^{-1}	−0.5–0.5	H_2SO_4	N/A	This work
$Ti_3C_2T_x$–SnO_2 NPs/PPy	Chemical oxidation	806.67	2.0 A g^{-1}	−0.5–0.5	H_2SO_4	98.3% over 10^4 GCD cycles	This work

show specific capacitances of 290.4, 447.5, 471.32, and 806.67 F g^{-1} at a 2 A g^{-1} current density. In Fig. 4(F), $Ti_3C_2T_x$–SnO_2 NPs/PPy shows a higher specific capacitance curve than that of PPy, $Ti_3C_2T_x$–PPy, and $Ti_3C_2T_x$–SnO_2 NPs. eqn (5) and (6) were used to calculate specific capacitance (C_{sp}) from the CV and GCD curves, respectively:[70]

$$\text{CV based}: \quad C_{sp} = \frac{\int I(V)\mathrm{d}V}{vm\Delta V} \tag{5}$$

$$\text{GCD based}: \quad C_{sp} = \frac{I\Delta t}{m\Delta V} \tag{6}$$

where $\int I(V)\mathrm{d}V$ is the constrained area under the CV curve under the current in (A), ΔV is the potential window or cut-off voltage in (V), I is the instant discharge current value in (A), v is the scan rate in (mV s^{-1}), m represents the mass of the electrode materials in grams, and Δt denotes the discharge time in seconds.

This highlights the fact that $Ti_3C_2T_x$–SnO_2 NPs/PPy modified is a highly capacitive supercapacitor electrode. The Nyquist plot for $Ti_3C_2T_x$–SnO_2 NPs/PPy and the Bode plot for the phage angle are displayed in Fig. 4(G and H). The Nyquist plot displayed in Fig. 4(G), shows an upper trending linear diagram without a semicircle. The Bode plot of the phage angle *versus* log(frequency) shown in Fig. 4(H) presents the maximum phage angle of 83.37°, which is near the ideal capacitive (−85°) nature of $Ti_3C_2T_x$–SnO_2 NPs/PPy electrode. Furthermore, the $Ti_3C_2T_x$–SnO_2 NPs/PPy modified electrode shows 98.3% stable performance after 10 000 consecutive cycles as presented in Fig. 4(I). The GCD stability graph at the end of 10 000 cycles is shown in Fig. S(5). The stability of GCD was driven at the current density of 4.0 A g^{-1}. A comparison of the supercapacitor performance of this work and previously published $Ti_3C_2T_x$/PPy-based electrodes are summarized in Table 1.

3.5. Electrochemical mechanism of *K. pneumoniae* detection

The link between the structural and compositional characterization of the nanocomposite with its functional performance, particularly in biosensing and electrochemical energy storage, is explained through Scheme 2(A and B). In Scheme 2A, the arrangement of $Ti_3C_2T_x$, SnO_2 NPs, and PPy is presented, where SnO_2 NPs are inserted in $Ti_3C_2T_x$ and PPy is covered on $Ti_3C_2T_x$–SnO_2 NPs. Thus, the successful formation of $Ti_3C_2T_x$–SnO_2 NPs/PPy nanocomposite was characterized *via* electrochemical testing for biosensors and their capacitive nature through supercapacitor properties studies. Additionally, in Scheme 2B, electrochemical charging alters the electrical properties of the modified surface. These changes influence how effectively bacteriophages can attach and bind to the surface. Thereafter, the phage can attack the *K. pneumoniae*, and the binding bacterial concentration is calculated by using electrochemical EIS and DPV techniques. This work explores the nanocomposite of $Ti_3C_2T_x$, SnO_2 NPs, and PPy for dual applications in biosensing and electrochemical energy storage.[76]

The composite leverages the individual properties of each component: $Ti_3C_2T_x$ for conductivity and surface area, SnO_2 NPs for enhanced electrochemical interaction, and PPy for

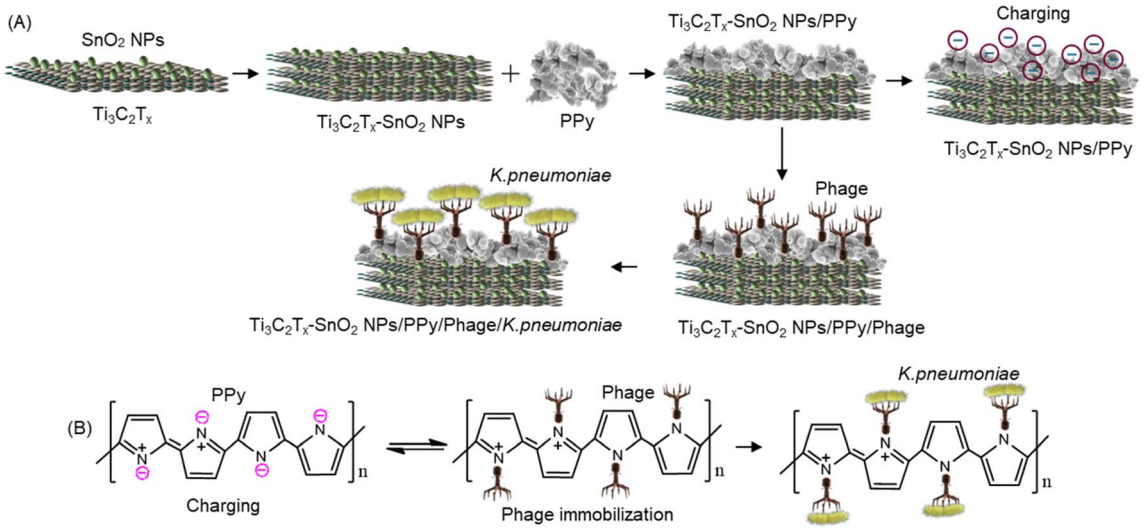

Scheme 2 (A) electrochemical mechanism of $Ti_3C_2T_x$–SnO_2 NPs/PPy nanocomposite formation towards biosensor and electrochemical capacitor, (B) mechanism of PPy in biosensor and electrochemical capacitor.

electroactivity and charge transport, leading to a material capable of both biosensing and electrochemical capacitive functionality.[77] The study investigates the electrochemical mechanisms of negative ion attachment and phage immobilization on the electrode surface as capacitive phenomena to optimize the dual functionality of the nanocomposite.

3.6. Electrochemical detection of *K. pneumoniae*

The analytical performance of $Ti_3C_2T_x$–SnO_2 NPs/PPy nanocomposites depends on their building block materials, like SnO_2 NPs, $Ti_3C_2T_x$, and PPy. Here, the analytical performance is tested in standard $[Fe(CN)_6]^{3-/4-}$ solution by DPV and EIS techniques. The DPV experiment was conducted at potential window of 0–0.5 V. EIS was operated at a wide frequency range, from as low as 10^{-1} Hz to as high as 10^6 Hz. With the optimized immobilization protocol, prepared SPE/$Ti_3C_2T_x$–SnO_2 NPs/PPy/Phage was infected with multiple concentrations of *K. pneumoniae*. Host bacterial concentrations were 10^1, 10^2, 10^3, 10^4, 10^5, and 10^6 CFU mL^{-1}. After bacterial immobilization on SPE/$Ti_3C_2T_x$–SnO_2 NPs/PPy/Phage, the electrode was used for DPV

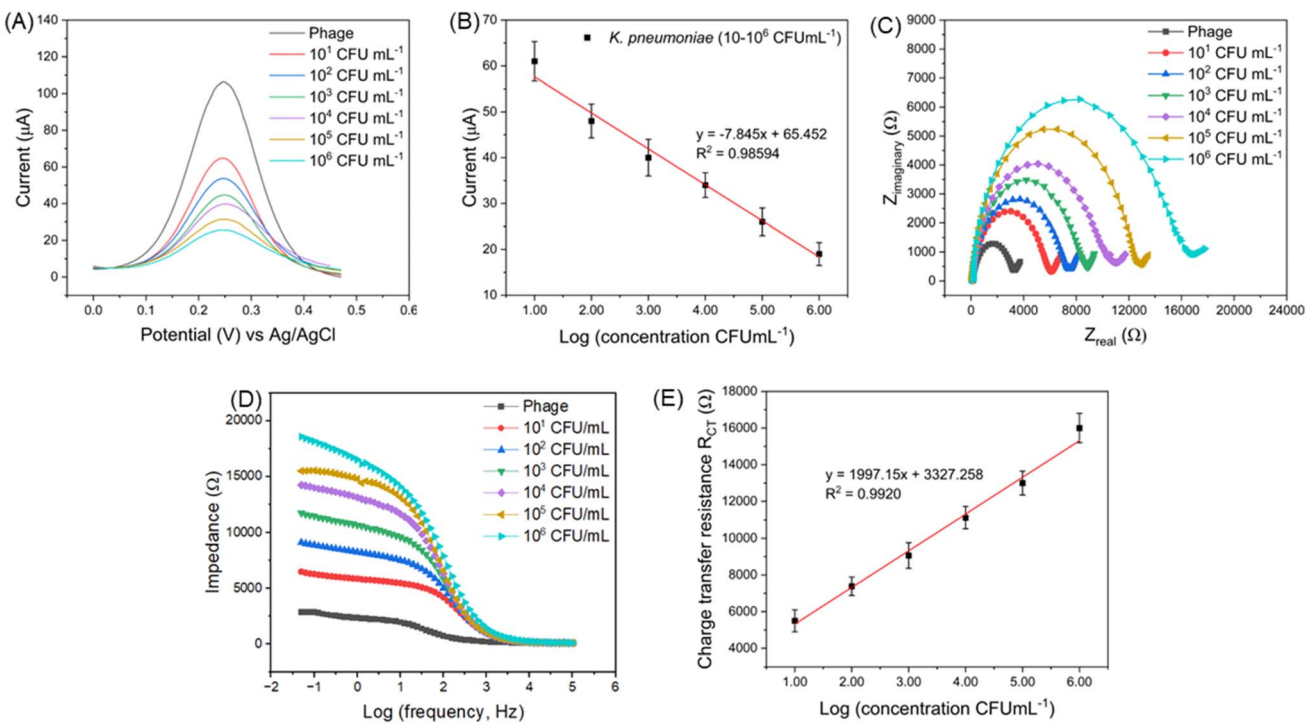

Fig. 5 (A) DPV and (B) calibration plot; (C) Nyquist, (D) Bode, and (E) calibration plot of SPE/$Ti_3C_2T_x$–SnO_2 NPs/PPy/Phage biosensor-based detection of 10^1, 10^2, 10^3, 10^4, 10^5, and 10^6 CFU mL^{-1} of *K. pneumoniae*.

anodic oxidation and EIS non-Faradic impedance measurement in $[Fe(CN)_6]^{3-/4-}$. The respective data are plotted in Fig. 5(A–E). In the DPV plot, a linear dynamic range of 10–10^6 CFU mL^{-1} was maintained with the corresponding regression equation of $y = -7.845x + 65.452$, and R^2 value of 0.98594, as shown in Fig. 5(A and B). The bacteria-infected electrode surface impedance was measured using EIS in the same $[Fe(CN)_6]^{3-/4-}$.

The corresponding Nyquist plot and Bode plot of impedance spectra are shown in Fig. 5(C–E). The R_{ct} value shows a linearity with the regression equation. In both DPV and EIS, it appears that the peak current is decreased with increasing bacterial concentration in DPV; in contrast, the diameter of a semicircle of the Nyquist plot grew with increasing *K. pneumoniae* concentrations 10–10^6 CFU m L^{-1}. A comparison of phage-modified electrochemical biosensors between this work and previously published research for *K. pneumoniae* quantification is summarized in Table 2.

3.7. Selectivity, repeatability, stability, and practical application

To evaluate the performance of the $Ti_3C_2T_x$–SnO_2 NPs/PPy electrode-based biosensor, a series of experiments were conducted to assess the selectivity, repeatability, stability, and real sample analysis. DPV measurements were carried out after attacking several bacteria (*S. typhi*, *E. coli* DH5α, *P. aeruginosa*, *E. coli* 0157:H7, *S. flexneri*, *V. cholerae*, *S. enterica*, *L. monocytogenes*) onto the SPE/$Ti_3C_2T_x$–SnO_2 NPs/PPy/Phage to study the biosensor's selectivity, and the results are presented in Fig. S6(A). The targeted host *K. pneumoniae* (10^3 CFU mL^{-1}) attacked the SPE/$Ti_3C_2T_x$–SnO_2 NPs/PPy/Phage modified electrode, and in DPV response, a 34 μA oxidation signal is recorded. On the contrary, the non-target host is not attacked on SPE/$Ti_3C_2T_x$–SnO_2 NPs/PPy/Phage, and the DPV response remains around 100 μA oxidation signal. So, the results can reveal that the biosensor can quantify *K. pneumoniae* with superior selectivity in the presence of many other interfering bacterial cells. Reproducibility is a key parameter for assessing the precision of electrochemical biosensors, primarily reflecting the stability of the biosensor itself. The precision of the biosensor was assessed by measuring its response five times at a *K. pneumoniae* concentration of 10^4 CFU mL^{-1}, as shown in Fig. S6(B).

To evaluate the stability of the SPE/$Ti_3C_2T_x$–SnO_2 NPs/PPy biosensor, the electrodes were stored at 4 °C. Every seven days, the functionalized electrodes were refreshed by introducing *K. pneumoniae* (10^3 CFU mL^{-1}) and immobilizing the phage. DPV measurements were then performed, and the findings are displayed in Fig. S6(C). These findings demonstrate the impact of storage duration on the stability of the developed biosensor. The stability reaches 98.1% after eleven consecutive weeks with a gradual decrease in the activity of $Ti_3C_2T_x$–SnO_2 NPs/PPy nanocomposite modified electrode. This indicates that, compared to previously reported phage-modified electrochemical biosensors, the biosensors developed in this study demonstrate superior stability.[13,79] To confirm the practical application of the developed biosensors as an effective diagnostic tool for monitoring *K. pneumoniae*, a recovery test was conducted in environmental samples (soil, agricultural water, hospital effluent, tap water, and urine). The collected data is presented in Table 3. To prepare a real sample, the bacteria were combined with an environmental sample and extracted using the procedure described in Subsection 2.4.1. The whole protocol was similarly maintained for the quantification of *K. pneumoniae*. The recovery efficiency of the designed SPE/$Ti_3C_2T_x$–SnO_2 NPs/PPy/Phage biosensor was outstanding, ranging from 99.75 to 99.90%. Despite the presence of background bacterial interference in the environmental sample, *K. pneumoniae* detection remained highly reliable and consistent.

Table 3 Recovery test of *K. pneumoniae* in soil, agricultural water, hospital effluent, tap water, and urine using the proposed biosensor

Sample name	Add (CFU mL^{-1})	Detected (CFU mL^{-1})	Recovery (%)
Soil	10^4	9975	99.75
Agricultural water	10^4	9990	99.90
Hospital effluent	10^4	9980	99.80
Tap water	10^4	9993	99.93
Urine	10^4	9988	99.88

Table 2 Comparison of phage-modified electrochemical biosensors for the detection of *K. pneumoniae*[a]

Electrodes	Modification type	Target bacteria	Assay type	Detection range (CFU mL^{-1})	LOD (CFU mL^{-1})	Sample	Ref.
BC/c-MWCNT/PEI	CL	*Staphylococcus aureus*	DPV	3.0–3.0 × 10^7	3.0	PBS	78
				5.0–5.0 × 10^6	5.0	Milk	78
PEI/c-CNT	EI	*Staphylococcus aureus*	EIS	10^2–10^7	1.23 × 10^2	Water	13
					1.23 × 10^2	Blood plasma	
PAN-derived CNF	EI	*Escherichia coli*	EIS	10^2–10^6	36	PBS, apple juice	18
AuE/11-MUA-3MPA/NHS-EDC	EI	*Escherichia coli*	DPV	1.9 × 10^1–1.9 × 10^8	14 ± 5	SM buffer	14
$Ti_3C_2T_x$–SnO_2 NPs/PPy	EI	*K. pneumoniae*	DPV, EIS	10–10^6	1.0	PBS	This work

[a] Abbreviations: BC: bacterial cellulose, c-MWCNT: carboxylated multiwalled carbon nanotube, PEI: polyethyleneimine, PAN: poly-acetonitrile; CNF: carbon nanofibre, 11-MUA: 11-mercaptoundecanoic acid, 3-MPA: 3-mercaptopropionic acid, NHS: *N*-hydroxy-succinimide, EDC: 1-ethyl-3-(3-dimethylaminopropyl) carbodiimide hydrochloride.

4 Conclusion

Herein, a capacitive electrochemical biosensor electrode based on a $Ti_3C_2T_x$–SnO_2 NPs/PPy nanocomposite for bacteriophage immobilization and the selective detection of *K. pneumoniae* was successfully engineered. The fabricated $Ti_3C_2T_x$–SnO_2 NPs/PPy electrode exhibited capacitive behavior, with a *b*-value of 0.830 derived from the power law equation and a 90% capacitive contribution at a scan rate of 10 mV s^{-1}, as determined using the Dunn method. Comparative evaluation of individual and binary components PPy, $Ti_3C_2T_x$–PPy, $Ti_3C_2T_x$–SnO_2 NPs, and $Ti_3C_2T_x$–SnO_2 NPs/PPy revealed *b*-values of 0.656, 0.456, and 0.962, and corresponding specific capacitances of 290.4, 447.5, and 471.32 F g^{-1}, respectively. Remarkably, the $Ti_3C_2T_x$–SnO_2 NPs/PPy nanocomposite achieved an elevated specific capacitance of 806.67 F g^{-1} and a phase angle of −83.37°, closely approximating the ideal capacitive response (−85°). These findings confirm the capacitive nature and superior electrochemical performance of the $Ti_3C_2T_x$–SnO_2 NPs/PPy modified electrode. Upon immobilization of bacteriophages, the resulting $Ti_3C_2T_x$–SnO_2 NPs/PPy/Phage biosensor demonstrated efficient detection of *K. pneumoniae* using DPV and EIS techniques, covering a dynamic linear detection range of 10–10^6 CFU mL^{-1}. The practical applicability of the developed sensor was validated using complex real-world samples, including soil, agricultural water, hospital effluent, and urine matrices. Overall, the $Ti_3C_2T_x$–SnO_2 NPs/PPy/Phage biosensor offers a promising platform for both environmental surveillance and clinical diagnostics, owing to its high sensitivity, stability, and adaptability to diverse sample types. This is the first to report on PPy-based functionalized capacitive electrochemical detection of *K. pneumoniae*.

Ethics approval

Healthy urine samples were collected from healthy donors, who provided written informed consent for this study according to the Declaration of Medical Services. The blood drawing and experimental procedures were performed in accordance with the Guidelines for Care and Use of Human Samples of Jashore University of Science and Technology (JUST) and approved by the Medical Ethics Committee of Jashore-7408, Bangladesh.

Author contributions

Md. Abdul Khaleque: electrode fabrication, data collection, analysis, writing original draft, review and editing; Moumita Rahman: bacteriophage and bacteria culture, and writing original draft; Selina Akter: methodology, data analysis, and writing original draft; Md. Romzan Ali: data analysis, review and editing; Syed Imdadul Hossain: methodology, investigation, and review and editing; Rahman Saidur: $Ti_3C_2T_x$ synthesis, reviewing and editing; Mohamed Aly Saad Aly: conceptualization, methodology, analysis and discussion, supervision, project management, and reviewing and editing; Md. Zaved H. Khan: conceptualization, methodology, review and editing, and supervision.

Conflicts of interest

The authors declare that there is no conflict of interest.

Data availability

The datasets used and analyzed during the current study are available from the corresponding author upon reasonable request.

Supplementary information is available. See DOI: https://doi.org/10.1039/d5ra03642a.

Acknowledgements

This work received specific funding from Georgia Tech Shenzhen Institute (GTSI) and Jashore University of Science and Technology.

References

1 C. L. Gorrie, M. Mirčeta, R. R. Wick, L. M. Judd, M. M. C. Lam, R. Gomi, I. J. Abbott, N. R. Thomson, R. A. Strugnell, N. F. Pratt, J. S. Garlick, K. M. Watson, P. C. Hunter, D. V. Pilcher, S. A. McGloughlin, D. W. Spelman, K. L. Wyres, A. W. J. Jenney and K. E. Holt, *Nat. Commun.*, 2022, **13**, 3017, DOI: 10.1038/s41467-022-30717-6.

2 A. G. Elliott, D. Ganesamoorthy, L. Coin, M. A. Cooper and M. D. Cao, *Genome Announc.*, 2016, **4**(3), e00438, DOI: 10.1128/genomeA.00438-16.

3 D. Chang, L. Sharma, C. S. Dela Cruz and D. Zhang, *Front. Microbiol.*, 2021, **12**, 750662, DOI: 10.3389/fmicb.2021.750662.

4 Z. Zhang, H. W. Yu, G. C. Wan, J. H. Jiang, N. Wang, Z. Y. Liu, D. Chang and H. Z. Pan, *J. AOAC Int.*, 2017, **100**, 548–552.

5 N. Florien, S. Sharma, D. Kala, S. Gupta, A. Kaushal and D. Kumar, *Discov. Life*, 2025, **55**(1), 1–12.

6 M. R. Ali, M. S. Bacchu, M. A. A. Setu, S. Akter, M. N. Hasan, F. T. Chowdhury, M. M. Rahman, M. S. Ahommed and M. Z. H. Khan, *Biosens. Bioelectron.*, 2021, **188**, 113338, DOI: 10.1016/j.bios.2021.113338.

7 M. S. Bacchu, M. R. Ali, S. Das, S. Akter, H. Sakamoto, S. I. Suye, M. M. Rahman, K. Campbell and M. Z. H. Khan, *Anal. Chim. Acta*, 2022, **1192**, 339332, DOI: 10.1016/j.aca.2021.339332.

8 H. A. Hussein, A. Kandeil, M. Gomaa and R. Y. A. Hassan, *Microsyst. Nanoeng.*, 2023, **9**, 105, DOI: 10.1038/s41378-023-00578-0.

9 N. Gupta, in *Journal of Cytology*, Wolters Kluwer Medknow Publications, 2019, vol. 36, pp. 116–117.

10 Y. Ding, Y. Zhang, C. Huang, J. Wang, H. Li and X. Wang, *Talanta*, 2024, **270**, 125561.

11 Y. Zhou, A. Marar, P. Kner and R. P. Ramasamy, *Anal. Chem.*, 2017, **89**, 5734–5741.

12 N. Bhardwaj, S. K. Bhardwaj, J. Mehta, G. C. Mohanta and A. Deep, *Anal. Biochem.*, 2016, **505**, 18–25.

13 D. Patel, Y. Zhou and R. P. Ramasamy, *J. Electrochem. Soc.*, 2021, **168**, 057523.
14 J. Xu, C. Zhao, Y. Chau and Y. K. Lee, *Biosens. Bioelectron.*, 2020, **151**, 111914, DOI: 10.1016/j.bios.2019.111914.
15 Å. Richter, K. Matuła, A. Leśniewski, K. Kwaśnicka, J. Łoś, M. Łoś, J. Paczesny and R. Hołyst, *Sens. Actuators, B*, 2016, **224**, 233–240.
16 I. U. Haq, K. Rahim, S. Maryam and N. P. Paker, *Biotech. Rep.*, 2025, **45**, e00872, DOI: 10.1016/j.btre.2024.e00872.
17 U. Farooq, M. W. Ullah, Q. Yang, A. Aziz, J. Xu, L. Zhou and S. Wang, U. Farooq, M. W. Ullah, Q. Yang, A. Aziz, J. Xu, L. Zhou and S. Wang, *Biosens. Bioelectron.*, 2020, **157**, 112163, DOI: 10.1016/j.bios.2020.112163.
18 Y. L. Wang, L. Q. Fan, S. J. Sun, J. J. Chen, Z. X. Wu, T. T. Zhu, Y. F. Huang and J. H. Wu, *Chem. Eng. J.*, 2022, **428**, 131993.
19 I. B. Qader, H. K. Ismail, H. F. Alesary, J. H. Kareem, Y. T. Maaroof and S. Barton, *J. Electroanal. Chem.*, 2023, **951**, 117943.
20 L. Lan, Y. Li, J. Zhu, Q. Zhang, S. Wang, Z. Zhang, L. Wang and J. Mao, *Chem. Eng. J.*, 2023, **455**, 140675.
21 Ö. Yavuz, M. K. Ram, M. Aldissi, P. Poddar and H. Srikanth, *Synth. Met.*, 2005, **151**, 211–217.
22 W. A. El-Said, O. Nasr, A. I. A. Soliman, E. A. Elshehy, Z. A. Khan and F. K. Abdel-Wadood, *Appl. Surf. Sci. Adv.*, 2021, **4**, 100065, DOI: 10.1016/j.apsadv.2021.100065.
23 F. Liu, Y. Yuan, L. Li, S. Shang, X. Yu, Q. Zhang, S. Jiang and Y. Wu, *Composites, Part B*, 2015, **69**, 232–236.
24 M. A. Khaleque, M. Aly Saad Aly and M. Z. H. Khan, *Chem. Eng. J.*, 2025, **507**, 160444, DOI: 10.1016/j.cej.2025.160444.
25 H. Ding, M. Zhang, Y. Liu, Y. Yao, Z. Mai, H. Zheng, B. Song, B. Fan, H. Wang and H. Lu, *Ceram. Int.*, 2024, **50**, 46334–46346.
26 K. Tian, X. Hui, H. Wang, Z. Zhang, L. Zhang, C. Wang and L. Yin, *Electrochim. Acta*, 2022, **415**, 140242.
27 R. Shafique, M. Rani, K. Batool, A. A. Alothman, M. S. Saleh Mushab, A. A. Shah, A. Kanwal, S. Ali and M. Arshad, *J. Mater. Res. Technol.*, 2023, **24**, 2668–2677.
28 X. Liu, Y. Chen, H. Zhang, L. Zhuo, Q. Huang, W. Zhang, H. Chen and Q. Ling, *J. Colloid Interface Sci.*, 2024, **660**, 735–745.
29 E. Azizi, J. Arjomandi, H. Shi and M. A. Kiani, *J. Energy Storage*, 2024, **75**, 109665, DOI: 10.1016/j.est.2023.109665.
30 D. Li, H. Liang and Y. Zhang, *Carbon*, 2024, **226**, 119205.
31 T. K. Paul, M. A. Khaleque, M. R. Ali, M. Aly Saad Aly, M. S. Bacchu, S. Rahman and M. Z. H. Khan, *RSC Adv.*, 2025, **15**(12), 8948–8976, DOI: 10.1039/d5ra00271k.
32 W. Zhao, Y. Lei, Y. Zhu, Q. Wang, F. Zhang, X. Dong and H. N. Alshareef, *Nano Energy*, 2021, **86**, 106120, DOI: 10.1016/j.nanoen.2021.106120.
33 N. Zhao, Y. Yang, D. Yi, Y. Xiao, K. Wang, W. Cui and X. Wang, *Chem. Eng. J.*, 2021, **422**, 130018, DOI: 10.1016/j.cej.2021.130018.
34 Q. Lu, C. Liu, Y. Zhao, W. Pan, K. Xie, P. Yue, G. Zhang, A. Omar, L. Liu, M. Yu and D. Mikhailova, *SusMat*, 2023, **3**, 471–497.
35 D. Liang, P. Song, M. Liu and Q. Wang, *Ceram. Int.*, 2022, **48**, 9059–9066.
36 M. Cao, S. Liu, S. Liu, Z. Tong, X. Wang and X. Xu, *Microchem. J.*, 2022, **175**, 107068.
37 A. P. S. GAHLOT, R. Pandey, S. Singhania, A. choudhary, A. Garg and P. M. Gupta, Evolution of tin oxide (SnO2) nanostructures synthesized by hydrothermal method, 2021, DOI: 10.21203/rs.3.rs-1097943/v1.
38 B. Dharmasiri, K. A. S. Usman, S. A. Qin, J. M. Razal, N. T. Tran, P. Coia, T. Harte and L. C. Henderson, *Chem. Eng. J.*, 2023, **476**, 146739, DOI: 10.1016/j.cej.2023.146739.
39 M. R. Lukatskaya, O. Mashtalir, C. E. Ren, Y. Dall'Agnese, P. Rozier, P. L. Taberna, M. Naguib, P. Simon, M. W. Barsoum and Y. Gogotsi, *Science*, 2013, **341**, 1502–1505.
40 M. Hu, Z. Li, T. Hu, S. Zhu, C. Zhang and X. Wang, *ACS Nano*, 2016, **10**(12), 11344–11350, DOI: 10.1021/acsnano.6b06597.
41 L. Tong, C. Jiang, K. Cai and P. Wei, *J. Power Sources*, 2020, **465**, 228267, DOI: 10.1016/j.jpowsour.2020.228267.
42 C. Zhao, Z. Wei, J. Zhang, P. He, X. Huang, X. Duan, D. Jia and Y. Zhou, *J. Alloys Compd.*, 2022, **907**, 164428, DOI: 10.1016/j.jallcom.2022.164428.
43 M. A. Khaleque, M. R. Ali, M. Aly Saad Aly, M. I. Hossain, K. H. Tan, M. A. Zaed, R. Saidur, M. M. Rahman, N. M. Mubarak and M. Z. H. Khan, *Diamond Relat. Mater.*, 2024, **15**, 111749, DOI: 10.1016/j.diamond.2024.111749.
44 Y. Kang, Z. Li, K. Xu, X. He, S. Wei and Y. Cao, *J. Alloys Compd.*, 2019, **779**, 728–734.
45 L. Tan, L. Wang and Y. Wang, Hydrothermal synthesis of SnO 2 nanostructures with different morphologies and their optical properties, *J. Nanomater.*, 2011, **2011**(1), 529874, DOI: 10.1155/2011/529874.
46 Y. Zhao, J. Liu, Q. Liu, Y. Sun, D. Song, W. Yang, J. Wang and L. Liu, *Mater. Lett.*, 2014, **136**, 286–288.
47 M. Sravanthi and K. G. Manjunatha, in *Materials Today: Proceedings*, Elsevier Ltd, 2020, vol. 46, pp. 5964–5968.
48 A. Yussuf, M. Al-Saleh, S. Al-Enezi and G. Abraham, *Int. J. Polym. Sci.*, 2018, **2018**, 4191747, DOI: 10.1155/2018/4191747.
49 J. Parayangattil Jyothibasu, M. Z. Chen and R. H. Lee, *ACS Omega*, 2020, **5**, 6441–6451.
50 M. R. Ali, M. S. Bacchu, D. D. Ridoy, P. L. Mozumder, M. N. Hasan, S. Das, M. F. H. Palash, S. Akter, N. Sakib, A. Khaleque, D. Chakrobortty and M. Z. H. Khan, *RSC Adv.*, 2022, **12**, 31497–31505.
51 F. Zhang, W. Liu, S. Wang, C. Liu, H. Shi, L. Liang and K. Pi, *Composites, Part B*, 2021, **217**, 108900, DOI: 10.1016/j.compositesb.2021.108900.
52 S. Z. Shahanshahi and S. Mosivand, *Appl. Phys. A:Mater. Sci. Process.*, 2019, **125**, 652, DOI: 10.1007/s00339-019-2949-2.
53 Y. Fu and A. Manthiram, *RSC Adv.*, 2012, **2**, 5927–5929.
54 G. Kulkarni, P. Kandesar, N. Velhal, H. Kim and V. Puri, *J. Appl. Polym. Sci.*, 2021, **138**(22), 50447, DOI: 10.1002/app.50447.
55 R. Turczyn, K. Krukiewicz, A. Katunin, J. Sroka and P. Sul, *Compos. Struct.*, 2020, **232**, 111498, DOI: 10.1016/j.compstruct.2019.111498.
56 E. Smidt and K. Meissl, *Waste Manage.*, 2007, **27**, 268–276.

57 V. A. Lorenz-Fonfria, *Chem. Rev.*, 2020, **120**(7), 3466–3576, DOI: 10.1021/acs.chemrev.9b00449.
58 M. Naguib, M. Kurtoglu, V. Presser, J. Lu, J. Niu, M. Heon, L. Hultman, Y. Gogotsi and M. W. Barsoum, *Adv. Mater.*, 2011, **23**, 4248–4253.
59 A. Debataraja, D. W. Zulhendri, B. Yuliarto, H. Nugraha and B. Sunendar, in *Procedia Engineering*, Elsevier Ltd, 2017, vol. 170, pp. 60–64.
60 T. Preethi, K. Senthil, S. Ashokan, R. Balakrishnaraja, B. Sundaravel and P. Saravanan, *J. Nano- Electron. Phys.*, 2021, **13**, 1–5.
61 C. Z. Brusamarello, L. M. Santos, A. P. Romio, M. Di Domenico, A. F. Santos, P. H. H. de Araújo and C. Sayer, *Mater. Today Commun.*, 2021, **26**, 101740, DOI: 10.1016/j.mtcomm.2020.101740.
62 N. Khan, R. Ullah, M. Khan and Almas, *Electrochim. Acta*, 2024, **505**, 144988, DOI: 10.1016/j.electacta.2024.144988.
63 S. Dhineshkumar, E. Elanthamilan, S.-F. Wang, S. Rajkumar and J. P. Merlin, *Electrochim. Acta*, 2025, **512**, 145525.
64 D. Liang, P. Song, M. Liu and Q. Wang, *Ceram. Int.*, 2022, **48**, 9059–9066.
65 S. F. Tseng, S. J. Cheng, W. T. Hsiao, S. H. Hsu and C. C. Kuo, *Ceram. Int.*, 2024, **50**, 43728–43737.
66 P. Sharma and V. Kumar, *Mater. Today: Proc.*, 2020, **33**, 1573–1578.
67 K. Krishnamoorthy, P. Pazhamalai, V. K. Mariappan, S. Manoharan, D. Kesavan and S. J. Kim, *Adv. Funct. Mater.*, 2021, **3**(10), 2008422, DOI: 10.1002/adfm.202008422.
68 R. Anjana, P. M. Anjana, J. Alex, R. Isaac, R. S. S. Hussain and D. Sajan, *Diamond Relat. Mater.*, 2024, **146**, 111241, DOI: 10.1016/j.diamond.2024.111241.
69 A. A. Mohamad, *Inorg. Chem. Commun.*, 2025, **172**, 113677.
70 B. Karuppaiah, R. Sukanya, S. M. Chen, P. R. Chavan, R. Karthik, M. Hasan, A. Milton and J. J. Shim, *J. Energy Storage*, 2024, **79**, 110145.
71 M. Boota, B. Anasori, C. Voigt, M. Q. Zhao, M. W. Barsoum and Y. Gogotsi, *Adv. Mater.*, 2016, **28**, 1517–1522.
72 W. Zhang, J. Ma, W. Zhang, P. Zhang, W. He, J. Chen and Z. M. Sun, *Nanoscale*, 2020, **12**, 6637–6643.
73 T. A. Le, N. Q. Tran, Y. Hong and H. Lee, *Chem.—Eur. J.*, 2019, **25**, 1037–1043.
74 J. Cao, Y. Han, X. Zheng and Q. Wang, *J. Appl. Polym. Sci.*, 2019, **136**(4), 47003, DOI: 10.1002/app.47003.
75 L. Yang, F. Lin, F. Zabihi, S. Yang and M. Zhu, *Int. J. Biol. Macromol.*, 2021, **181**, 1063–1071.
76 A. Al Mahmud, A. H. Alshatteri, H. S. Alhasan, W. Al Zoubi, K. M. Omer and M. R. Thalji, *Electrochim. Acta*, 2024, **503**, 144857.
77 N. Neha and A. Dalvi, *RSC Adv.*, 2025, **15**, 6518–6530.
78 U. Farooq, M. W. Ullah, Q. Yang, A. Aziz, J. Xu, L. Zhou and S. Wang, *Biosens. Bioelectron.*, 2020, **157**, 112163, DOI: 10.1016/j.bios.2020.112163.
79 R. F. Wang and R. Wang, *Bioelectrochemistry*, 2022, **148**, 108229, DOI: 10.1016/j.bioelechem.2022.108229.